Spectral Line Advanced Topics

John M. Dickey

University of Minnesota, Department of Astronomy,
116 Church St. SE, Minneapolis, MN 55455 USA

Abstract.
    This chapter is in three parts. The first gives the fundamental equations of level populations and radiative transfer which govern spectral line emission and absorption. Lines in the cm-wave band have similarities which allow us to simplify the equations. The further simplification of a two level system (a good approximation for HI) gives the familiar formulae for the 21-cm line.

    The second part of the lesson deals with mapping, and the combination of single dish and interferometer data. We consider the effect of gridding single dish data using a convolving function. Mapping speeds and techniques are discussed.

    The third part discusses the spectral line cube and its moments. The use of the first moments to determine the dynamical structure of a disk is discussed. The need for windowing in the cube before computing moments is justified.

1.   Spectral Line Basics : Radiative Transfer

Spectral lines below 10 GHz come from transitions between quantum levels with miniscule energy separations; this is necessary if the photon energy is to be less than 4×10^{-5} ev, so that its frequency will be in this range. Atomic hydrogen has two ranges where the energy levels are so closely spaced : at very high quantum numbers ($n \gtrsim 80$) and in the ground state itself due to the hyperfine splitting. Several molecules also have transitions in this range, generally caused by similar hyperfine splitting of energy levels due to the magnetic moment of the nucleus, as in OH and H_2CO. The more important spectral lines with frequencies below 10 GHz are listed on table 1.

    Recombination lines are generated as an electron cascades down the energy levels of an atom; at cm-waves the transitions between levels with high quantum numbers are important. These make a comb of lines whose frequencies are given by the Rydberg formula,

$$\nu_{ul} \;=\; Z\,\frac{R_0}{1 + \frac{m_e}{M_{amu}}}\,\times\left(\frac{1}{l^2}\;-\;\frac{1}{u^2}\right) \tag{1}$$

where l and u are the quantum numbers of the lower and upper states of the transition, Z is the screened nuclear charge (i.e. the number of protons minus the

number of other electrons), M_{amu} is the atomic mass in amu (1.007825 for H), and m_e is the electron mass. The Rydberg constant, R_0 is 3.289842×10^{15} Hz (Rohlfs and Wilson, 1996, p. 316). Recombination lines always come in groups, with the hydrogen line slightly lower in energy than the corresponding He line, and the corresponding C (and heavier element) lines piling up at frequencies just slightly higher than He. A few examples of recombination lines are included on the lower half of table 1.

Table 1.   Some Spectral Lines with Frequencies Below 10 GHz

Transition	Rest Frequency (GHz)	A Recent Reference
HI	1.4204058	Gibson et al. 2000
OH	1.665402, 1.667385	Liszt and Lucas 1996
	1.61223, 1.720559	Lewis et al. 2001
OH	4.765562, 4.660242	Szymczak et al. 2000
CH	3.2638, 3.3355, 3.3492	Magnani and Onello 1993
H_2CO	4.82966	Pauls et al. 1996
OH	6.035092	Caswell 1997
CH_3OH	6.668518	Phillips et al. 1997
^{3}He	8.665	Bania et al. 1997
	A Few Recombination Lines	
H92α	8.309382	Lang et al. 2001
H109α	5.008923	Peck et al. 1997
H271α	0.3285959	Roshi and Anantharamaiah 1997
C271α	0.3287597	Roshi and Anantharamaiah 1997

1.1.   Level Populations

Line intensities are determined by the populations of the two quantum levels of the transition, which set the amount of emission and absorption at each point along the line of sight. Whether or not the excitations are in thermal equilibrium with the kinetic temperature of the gas, we can describe the ratio of the populations of the two levels using the Boltzmann equation with some temperature T_{ex}, as :

$$\frac{n_u}{n_l} \;=\; \frac{b_u}{b_l} \; \frac{g_u}{g_l} \; e^{\frac{-h\nu}{kT_{ex}}} \tag{2}$$

where n_u and n_l are the level populations of the upper and lower levels, g_u and g_l are the statistical weights of the two levels, $h\nu$ is the energy of the photon, k is Boltzmann's constant, and T_{ex} is a temperature which is equal to the kinetic temperature in the special case where the collision rate is high enough to thermalize the transition (Osterbrock 1989, section 3.5).

At cm-waves the photon energies are so low that we can usually make the approximation $\frac{h\nu}{kT_{ex}} \ll 1$; in that case we can expand the Boltzmann equation in a Taylor series :

$$\frac{n_u}{n_l} \;=\; \frac{g_u}{g_l} \; \times \left(1 \;-\; \frac{h\nu}{kT_{ex}} \;+\cdots\right) \tag{3}$$

For a two level system, i.e. one in which all the atoms are in one or the other of two levels, so that $n_u + n_l = n$, the first order term of the expansion makes the number in the upper level, n_u, just proportional to the total density, i.e.

$$n_u \;=\; n \times \frac{n_u}{n_u + n_l} \;=\; n \times \frac{\frac{n_u}{n_l}}{1 + \frac{n_u}{n_l}} \;\simeq\; n \times \frac{g_u}{g_u + g_l} \tag{4}$$

this gives $n_u \simeq \frac{3}{4} \times n$ for the hyperfine-spit levels of the HI ground state. The two level approximation is valid for atomic hydrogen when all the atoms are in the ground state, as in the cool phases of the interstellar medium.

1.2. Emission and Absorption

The emission and absorption coefficients can be derived once we know the level populations. Generally the emission coefficient, j_ν, is given by :

$$\int j_\nu \; d\nu \;=\; \frac{n_u \; A_{ul} \; h\nu}{4\pi} \tag{5}$$

where A_{ul} is the Einstein coefficient for spontaneous emission for the transition from level u to l. The frequency integrals are taken over the line profile (the subscript ν indicates that this is a function of frequency). The absorption coefficient is given by

$$\int I_\nu \; \kappa_\nu \; d\nu \;=\; h\nu \left(n_l B_{lu} \;-\; n_u B_{ul} \right) \frac{I_\nu}{c} \tag{6}$$

where I_ν is the radiation intensity and B_{lu} and B_{ul} are the Einstein coefficients which describe the probability of absorption and stimulated emission of a photon, respectively. These are in the ratio

$$B_{lu} \;=\; \frac{g_u}{g_l} B_{ul} \tag{7}$$

(Spitzer 1977, section 3.4).

Note that the units of the emission and absorption coefficients are different. For j_ν the units are erg cm^{-3} sec^{-1} Hz^{-1} sterrad^{-1}, which is just the energy in the radiation coming from a unit volume of gas per second, going into a unit bandwidth of the emission spectrum and into a unit solid angle in direction. The units of κ_ν are the same, divided by I_ν, since the absorption is always proportional to the intensity of the incident radiation field itself; this works out to give κ_ν simply units of cm^{-1}. Thus the combined effect of the emission and absorption of a differential volume element, ds, somewhere along the line of sight is to change the radiation intensity by dI where

$$dI_\nu \;=\; j_\nu \; ds \;-\; \kappa_\nu \; I_\nu \; ds \tag{8}$$

The ratio of the emission and absorption coefficients is the Plank source term :

$$\mathcal{B}_\nu \;=\; \frac{j_\nu}{\kappa_\nu} \tag{9}$$

$$=\; \frac{2h\nu^3}{c^2} \frac{1}{e^{h\nu/kT} - 1} \tag{10}$$

$$\simeq \ \frac{2kT}{\lambda^2} \tag{11}$$

where the approximation is the Rayleigh-Jeans law which defines the brightness temperature :

$$T_B \ = \ \frac{\mathcal{B}_\nu \ c^2}{2 \ k \ T \ \nu^2} \tag{12}$$

For a two level system with energy separation giving a cm-wave line, the emission coefficient is proportional to the density, using equation 3 in equation 5 gives:

$$\int j_\nu d\nu \ = \ \frac{g_u}{g_u + g_l} \ \frac{A_{ul} \ h\nu}{4\pi} \times n \tag{13}$$

For the absorption coefficient we must include the second term in the Taylor expansion in equation 3, since to first order the number of photons absorbed is just cancelled by the extra number produced through stimulated emission. Thus we get

$$\int \kappa_\nu d\nu = \frac{h\nu \ B_{ul}}{c \ g_l} \ (\ g_u n_l \ - \ g_l n_u) \tag{14}$$

$$= \ \frac{h\nu \ B_{ul} \ n_l}{c \ g_l} \left(g_u \ - \ g_l \frac{n_u}{n_l} \right) \tag{15}$$

$$= \ \frac{h\nu \ B_{ul} \ n_l}{c \ g_l} \left\{ g_u \ - \ g_l \left[\frac{g_u}{g_l} \left(1 - \frac{h\nu}{kT_{ex}} \right) \right] \right\} \tag{16}$$

$$= \ \frac{(h\nu)^2 \ B_{ul} \ n}{c \ k \ T_{ex}} \left(\frac{g_u}{g_u + g_l} \right) \tag{17}$$

1.3.   Radiative Transfer

When we integrate along the line of sight to determine what the telescope sees, the emission integral gives

$$I_\nu \ = \ \int j_\nu \ dx \ = \ \frac{A_{ul} \ h\nu}{4\pi} \frac{g_u}{g_u + g_l} \int n \ dx \tag{18}$$

or in brightness temperature units with Doppler velocity in place of frequency

$$\int T_B(v) \ dv \ = \ C_0 \times N \tag{19}$$

where $C_0 = 5.485 \times 10^{-19}$ K km s^{-1} cm^2 for the 21-cm line. Note that we have to take the velocity integral as well as the line of sight integral to determine the total column density, N, because the radial motions of the atoms give them slight Doppler shifts which generate a line profile in velocity or frequency. In the case of an unresolved object such as a distant galaxy, equation 19 gives the HI mass by

$$\frac{M_H}{m_\odot} \ = \ 2.3 \times 10^5 \ \left(\frac{d}{Mpc} \right)^2 \ \frac{\int S_v \ dv}{Jy \ kms^{-1}} \tag{20}$$

The corresponding integral of the absorption coefficient along the line of sight gives the optical depth :

$$\tau_\nu \;=\; \int \kappa_\nu \; dx \;=\; \frac{(h\nu)^2 \; B_{ul} \; n}{c \; k \; T_{ex}} \frac{g_u}{g_u + g_l} \int \frac{n}{T} \; dx \tag{21}$$

or for the velocity integral

$$\int \tau_v dv \;=\; C_0 \, \frac{N}{T_{harm}} \tag{22}$$

where again we replace the frequency integral with an integral over Doppler velocity, and C_0 for the 21-cm line has the same value as above. The T_{harm} in equation 21 is the harmonic mean temperature,

$$T_{harm} \;\equiv\; \frac{\int n \; dx}{\int \frac{n}{T_{ex}} \; dx} \tag{23}$$

This is only equal to the excitation temperature if the gas is isothermal along the line of sight.
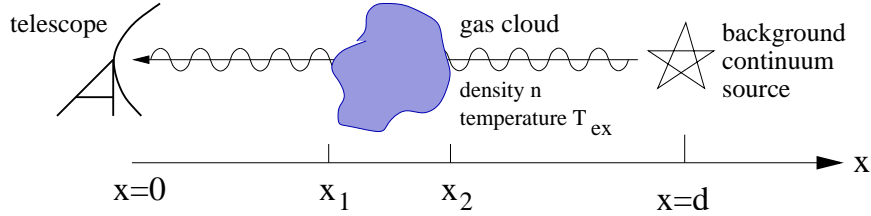

Figure 1. The geometry for the radiative transfer calculation in equations 29 - 31.

Once we have determined the emission and absorption coefficients we can use radiative transfer to calculate how the radiation intensity builds up through propagation along the line of sight, as shown in figure 1. Dividing equation 8 by κ_ν gives

$$\frac{dI_\nu}{d\tau_\nu} \;=\; -\frac{j_\nu}{\kappa_\nu} \;+\; I_\nu \tag{24}$$

since $d\tau = \kappa_\nu \; dx$ and $dx = -ds$, i.e. x increases away from the telescope, opposite the direction of propagation, ds. We can integrate this along the line of sight, $x = 0$ to distance d which translates to $\tau = 0$ to $\tau(d)$, after multiplying both sides by $e^{-\tau}$, i.e.

$$e^{-\tau_\nu} \frac{dI_\nu}{d\tau_\nu} \;-\; I_\nu e^{-\tau_\nu} \;=\; -\frac{j_\nu}{\kappa_\nu} \, e^{-\tau_\nu} \tag{25}$$

or

$$\frac{d}{d\tau_\nu} \left(e^{-\tau_\nu} \; I_\nu \right) \;=\; -\frac{j_\nu}{\kappa_\nu} \, e^{-\tau_\nu} \tag{26}$$

$$\int_{I(0)}^{I(d)} d\left(e^{-\tau} I_\nu \right) \;=\; -\int_0^{\tau(d)} \frac{j_\nu}{\kappa_\nu} \, e^{-\tau} \; d\tau \tag{27}$$

$$e^{-\tau(d)} I(d) \;-\; e^{-\tau(0)} I(0) \;=\; -\int_0^{\tau(d)} \frac{j_\nu}{\kappa_\nu} \, e^{-\tau} \; d\tau \tag{28}$$

Since we are starting at the telescope, $\tau(0) = 0$, so

$$I(0) = e^{-\tau(d)}I(d) + \int_0^{\tau(d)} \frac{j_\nu}{\kappa_\nu} e^{-\tau} d\tau \tag{29}$$

A simple case is that of a single cloud with a continuum background source, so that $\mathcal{B}_\nu(x) = \mathcal{B}_o$ inside the cloud (distance x_1 to x_2) and zero everywhere else, and $I(d) \equiv I_{bkg}$. Then

$$\tau = \int_{x_1}^{x_2} \kappa \, dx = \kappa(x_2 - x_1) = C_0 \times \frac{N}{T_{ex}} \tag{30}$$

where $N = n(x_2 - x_1)$ is the column density through the cloud, and the velocity integral has been taken on both sides. Then the received intensity of the radiation is

$$I_0 = \mathcal{B}_c \left(1 - e^{-\tau}\right) + I_{bkg} \, e^{-\tau} \tag{31}$$

where $\mathcal{B}_c$ is the Plank function for the excitation temperature of the gas in the cloud. In brightness temperature notation this is

$$T_B = T_{ex}\left(1 - e^{-\tau}\right) + T_{bkg} \, e^{-\tau}. \tag{32}$$

foreground warm gas   cool cloud   background warm gas   background continuum

N_f

column density N_c

temperature T_c N_b T_{cont}
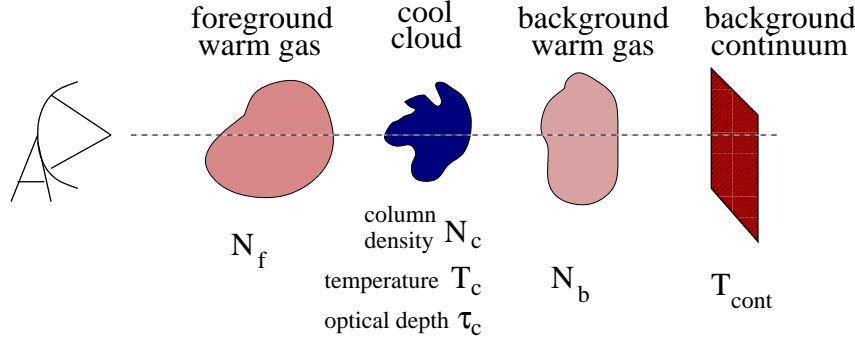
optical depth τ_c

Figure 2. The geometry for the radiative transfer calculation in equation 32.

A more complicated case is shown on figure 2, with optically thin foreground and background clouds of gas (column densities N_f and N_b) that are warm enough to have negligable optical depth, plus a cool, absorbing cloud with temperature T_c and column density N_c, plus background continuum, T_{cont}. This case gives

$$T_B(v) = \frac{C_0 \, N_f}{\sqrt{2\pi} \, \sigma_f} e^{\frac{(v-v_f)^2}{2\sigma_f^2}} + T_c \left(1 - e^{-\tau(v)}\right) +$$

$$+ \left(T_{cont} + \frac{C_0 \, N_b}{\sqrt{2\pi} \, \sigma_b} e^{\frac{(v-v_b)^2}{2\sigma_b^2}}\right) e^{-\tau(v)} \tag{33}$$

Here we assume that the shapes of the profiles are Gaussians with center velocities and dispersions (v_f, σ_f), (v_c, σ_c), and (v_b, σ_b) for the foreground, cloud, and background gas, respectively.

1.4. Velocity Profiles

In most areas of astronomy we use the optical version of the Doppler shift formula,

$$v_{radial} \equiv cz = c \times \frac{\Delta\lambda}{\lambda_r} \tag{34}$$

where $\Delta\lambda$ is the difference between the observed wavelength and the rest wavelength, λ_r. This defines the redshift, z, without any relativistic corrections, so that z can be greater than one. A useful formula to remember is that **the velocity range corresponding to one MHz of bandwidth is just equal to the wavelength in mm**. For the $\lambda 21.1$ cm line of HI this means that 1 MHz corresponds to 211 km s^{-1}, or 1 km s^{-1} is $\frac{1000}{211}$ kHz or 4.73 kHz.

For a Maxwellian distribution of velocities corresponding to a thermal gas with temperature T_{kin}, the line profile is Gaussian, and so j_ν, κ_ν, and I_ν all have frequency or Doppler velocity profiles following

$$I_v = I_0 \times e^{\left[-\frac{(v-v_0)^2}{2\sigma_v^2}\right]} \tag{35}$$

with

$$\sigma_v = \sqrt{\frac{2kT}{M_{amu}}}. \tag{36}$$

This reduces to

$$\sigma_v = 0.91 km s^{-1} \times \sqrt{\frac{T}{100K} \times \frac{1}{M_{amu}}} \tag{37}$$

for hydrogen, $\sigma_v \simeq 1$ km s^{-1} for gas at 120 K temperature, $\sigma_v \simeq 10$ km s^{-1} for gas at 12,000 K , and $\sigma_v \simeq 100$ km s^{-1} for gas at 1.2 million K.

2. Mapping Basics : The uv Plane

Whether we are observing with a single dish telescope, an aperture synthesis telescope, or a combination of the two, it is crucial to keep in mind the two Fourier conjugate representations of the telescope beam and the sky brightness. These are shown on figure 3, with the uv plane functions on the left, and their conjugate functions on the plane of the sky on the right. Since the aperture plane is the transform of the image plane, the telescope beam is the Fourier transform of the aperture illumination in both cases. But there is a fundamental difference between a single dish telescope (and/or an adding array interferometer) and a multiplying or correlation interferometer (aperture synthesis telescope). In the single dish case (shaded on the lower right of figure 3) it is the autocorrelation function of the illumination pattern which matters; the transform of this function is the beam power pattern. For the multiplying interferometer (shaded on the upper left of figure 3) the synthesized beam (dirty beam) is the transform of the illumination pattern itself. Thus there are negative sidelobes in the latter case, but not the former, since the autocorrelation function is always symmetric, so that its transform is real and positive definite.
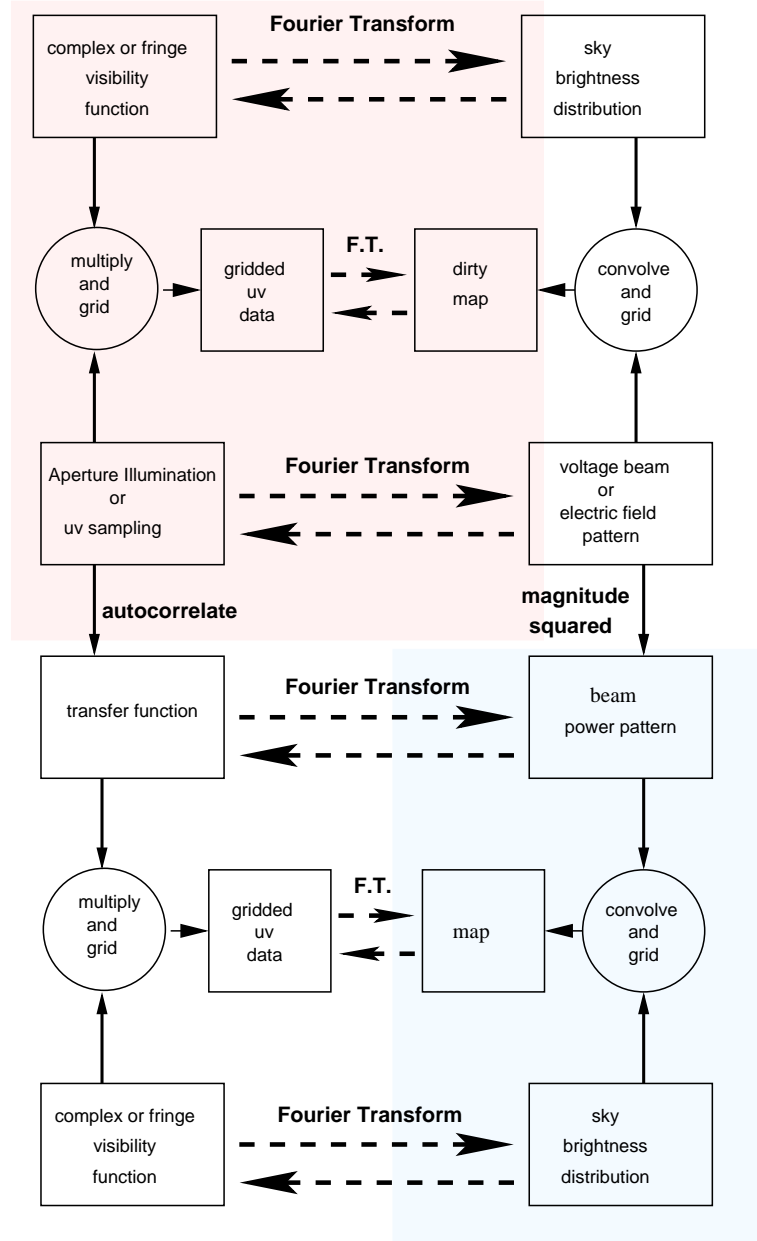
Figure 3. The relationship between the instrumental response and the sky brightness which lead to the measured map or image of the sky for two types of telescopes, aperture synthesis telescopes, i.e. correlation interferometers, (upper shaded area) and single dish telescopes or adding interferometers (lower shaded area). The left side is the uv plane, the right side is the lm or sky plane.

2.1. Gridding

An important step in the processing of either interferometer or single dish data is the gridding process. The Nyquist relation requires that the pixels in the map plane should be small enough that the FWHM of the beam is at least 2.4

pixels across, preferably 2.8 or more. If the pixels are larger than this relative to the beam width, then the higher spatial frequency information is lost due to undersampling. This is controlled in the aperture synthesis case by the gridding of the interferometer data on the uv plane before the transform back to the sky plane. When mapping with a single dish a similar gridding step is needed to make a map out of data taken either in separate pointings or "on-the-fly" while the telescope is driving. Even if the single dish observations are carefully taken in a lattice of pointings, it is still helpful to regrid the data using a convolving function which controls the behavior of the transform of the map. For example, noise in the spectra from the individual pointings can appear to have very high spatial frequencies, which alias on the uv plane back to low spatial frequencies unless they are suppressed by a convolving function in the gridding process. Thus the gridded map is :

$$T(x,y) \;=\; \frac{\Sigma_i T_i(l,m) f\left[(l-x),(m-y)\right]}{\Sigma_i U_i(l,m) f\left[(l-x),(m-y)\right]} \tag{38}$$

where the individual observations T_i are taken at positions (l,m) and the regular grid of the map pixels is given by (x,y). $f(x,y)$ is the convolving function, and $U(x,y)$ is a normalization function which is one at the positions of the observations. The division is suppressed for positions (x,y) so far from any observation that the denominator is less than some minimum threshold, typically between 0.2 and 0.05. A Gaussian is often used for f in the sky plane, in the uv plane it is better to use a exponential times sinc because of its aliasing suppression properties. If a Gaussian is used, the gridded map has resolution given by

$$FWHM^2_{gridded} \;=\; \sqrt{FWHM^2_{original} + FWHM^2_f} \tag{39}$$

The normalization illustrated in equation 37 by U has many variations, especially in aperture synthesis applications. The easiest to understand are "uniform weighting", in which each uv cell has the same weight regardless of the number of samples which contribute to it, and "natural weighting", in which each sample has the same weight, so that regions which are heavily sampled are weighted more highly than sparsely sampled regions. "Robust weighting" achieves some of the best features of both strategies. In any event, the gridding should provide pixels in the sky plane spaced by less than 1/2.4 times the FWHM of the telescope beam.

2.2. Mapping Speeds

For single dish mapping the speed depends on the desired sensitivity of the spectra. Using the radiometer equation :

$$\sigma_T = \frac{\sqrt{2}\; T_{sys}}{\sqrt{\delta\nu\; T_{int}}} \tag{40}$$

with $\delta\nu$ the channel bandwidth, T_{int} the integration time, and T_{sys} the system temperature, we get the rms noise, σ_T. The factor of $\sqrt{2}$ in the numerator is usually needed to account for calibration, e.g. frequency switching. For the example of on-the-fly mapping, we should drive the telescope and read out the

spectra so that one spectrum is read in the time it takes the telescope to move by less than 1/2.4 times the beamwidth, and so that this time provides σ_T less than 1/5 times the weakest features we hope to measure in the spectra after gridding. For Arecibo at 21-cm, this means we should read out spectra spaced by no more than about 1.2′. For channel bandwidth $\delta\nu$ of 0.5 km s^{-1} or 2.4 kHz we would need integration time per spectrum of 75 seconds to achieve rms noise of 100 mK, assuming system temperature of 30 K. Thus we can cover one square degree with 2600 spectra representing total integration time of 54 hours (plus overhead for telescope motion and calibration). So single dish mapping can be a slow process, even at such a modest sensitivity as this. The most common response to this is to undersample the beam, spacing the spectra further apart than the Nyquist condition requires. This compromises the quality of the map, particularly if it is to be combined with interferometer data. It also causes the gridded map to have an uneven sensitivity function, which is given by the noise divided by the normalization in equation 37, i.e.

$$ S(x,y) \;=\; \frac{\sigma_T}{\sqrt{\Sigma_i U_i(l,m)\; f\left[(l-x),(m-y)\right]}} \tag{41} $$

2.3.   Multibeam Surveys and Mosaicing

A very effective response to this problem is to build a multibeam receiver. An example is the Parkes 21-cm multibeam, which has been in use for more than four years on the 64m telescope of the Australia Telescope National Facility. Using just the seven inner beams a team of astronomers led by Naomi McClure-Griffiths have used this instrument to map the Southern Milky Way at 21-cm (McClure-Griffiths et al. 2000, 2001). This project is similar to a Northern Milky Way survey, the Canadian Galactic Plane Survey (CGPS, English et al. 1998, Normandeau et al. 1996). Both surveys combine single dish and aperture synthesis data to achieve high dynamic range, good resolution, and most of all uniform sensitivity to all angular scales from ∼1′ to many degrees.

Figure 4 indicates the telescope time required to survey a given area to a surface brightness sensitivity of 1 K (rms) in a velocity channel with width 0.8 km s^{-1}. The crosses mark single dish telescopes, while interferometers are marked with crescents which illustrate how tapering (weighting down the longest baselines) can improve the brightness sensitivity. Only a little tapering helps; tapering to beamwidths larger than about two times the untapered value decreases the brightness sensitivity because so much data is weighted down by the tapering function. In boxes on figure 4 are shown three future instruments. The Arecibo multibeam illustrates with the dashed arrow how much improvement in survey efficiency could be achieved if a seven beam system were installed on the AO telescope. The E array is a possible enhancement to the VLA which would concentrate the antennas even more densely than in the D array. The SKA is the Square Kilometer Array. The design of this telescope is not settled yet, but it will provide several orders of magnitude improvement in brightness sensitivity and resolution over any existing cm-wave telescope.

Figure 4. [*See the jpeg file associated with this paper.*] Mapping speeds with various telescopes. The resolution is indicated on the horizontal axis, while the number of square degrees per hour is on the vertical axis. The single dish telescopes (marked with crosses) would never be driven so fast as this figure suggests. Driving them more slowly (say, at 1 degree per hour) would give rms noise, σ_T, smaller than 1 K in proportion to the inverse square root of the effective integration time.

Large area surveys like the Southern Galactic Plane Survey (SGPS) and the CGPS using interferometer telescopes must make use of the technique of mosaicing. This observing strategy moves the pointing center frequently (typically every 30 seconds) over a raster of positions spaced by roughly the half width (FWHM/2) of the primary beam of the interferometer. These "snap-shot" observations are repeated many times to build up good uv coverage. This is a more effective use of telescope time than longer integration times per snap-shot, since the earth turns so slowly that most baselines do not change grid cells on the uv plane for many minutes. The more profound advantage of combining data from many nearby pointing centers of the interferometer is that it allows reconstruction of the shorter uv spacing information which cannot be directly measured because the antennas would shadow each other on such short baselines (Ekers and Rots, 1978, Cornwell 1985, Sault et al. 1995). The effect of mosaicing on the uv plane is to deconstruct the antennas, and give information for all baselines corresponding to the nearest bit of one antenna to the nearest bit of the next.

2.4. Combining Single Dish and Aperture Synthesis Data

Combining the data from the two types of telescopes can be done in a variety of ways. These were compared quantitatively using 21-cm data on the Small Magellanic Cloud by Stanimirović (1999). The basic alternatives are to combine the uv data before mapping, to combine dirty maps and jointly deconvolve the beam shapes (implemented in the Miriad task MOSMEM), and to deconvolve separately and combine the cleaned maps (implemented in the Miriad task IMMERGE). The last has given consistent and trustworthy results in many tests.

However they are combined, the relative calibration of the two sets of data is crucial. Generally single dish data is calibrated either using a standard brightness region (e.g. Weaver and Williams, 1973) which gives units of K for T_B, or by observing unresolved continuum sources of known flux density, which gives units of Jy per beam. Interferometer maps are always calibrated using unresolved sources, thus they also generally have units of Jy per beam. The two are related by the gain of the synthesized beam, i.e.

$$G \;=\; \frac{A_e}{k} \;=\; \frac{\lambda^2}{\Omega_B \; k} \tag{42}$$

where A_e is the effective area of the dish and Ω_B is the solid angle of the synthesized (clean) beam, i.e.

$$\Omega_B \;=\; 1.13 \; FWHM_1 \times FWHM_2 \tag{43}$$

where $FWHM_1$ and $FWHM_2$ are the major and minor axes of the clean beam. For these beam widths in arc minutes, the gain is

$$G \;=\; 169 \; K \; Jy^{-1} \, (FWHM_1 \times FWHM_2)^{-2} \tag{44}$$

This definition of the gain is $\frac{\lambda^2}{4\pi k}$ times the standard engineering quantity called the directive gain. The advantage of this definition is that it gives the conversion between units of Jy per beam and K of brightness temperature. For the Arecibo telescope at 21-cm $G \simeq 10$ K Jy^{-1}, for the GBT it may be about 1.5 K Jy^{-1}. For the VLA D-array with clean beam size of $45''$ the gain is 300 K Jy^{-1}. Using the gain, we can convert from the observed antenna temperature to the true flux density of the source, S. In the spectral line case, the analog of the brightness temperature integral of equation 19 becomes the flux integral ($\int S(v)\ dv\ =\ \frac{\int T_A(v)\ dv}{G}$). This gives the HI mass for the case of an unresolved 21-cm line source such as a distant galaxy,

$$\frac{M_H}{m_\odot}\ =\ 2.3 \times 10^5 \left(\frac{d}{Mpc}\right)^2 \frac{\int S(v)\ dv}{Jy\ kms^{-1}} \tag{45}$$

where d is the distance to the galaxy.

Figure 5. [*See the jpeg file associated with this paper.*] Images of part of a Galactic Supershell at longitude 277, latitude 0, velocity 38.75 km s^{-1}. The upper panel shows Parkes data only, the middle panel shows ATCA interferometer data only, and the lower panel shows the combined map.

Before the data can be combined the calibration scales of the two instruments must be matched carefully. The only sure way to do this is by comparing data for the same source **in the overlap region on the uv plane**, which is the range of spatial frequencies for which both instruments have good sensitivity. Such an overlap calibration is implemented in the Miriad task `IMMERGE`.

Figure 5 shows the combination of single dish and interferometer maps of the edge of a supershell in the outer Milky Way HI (McClure-Griffiths et al. 1999). The range of uv spacings contributing to each is manifest in its appearance. Only by combining them is the full range of structure clear.

3. Using Spectral Line Cubes

The spectral line cube is a three dimensional data structure made by stacking maps taken at different frequencies, i.e. Doppler velocities. The cube can be represented as a movie, either as a series of images of the sky at different frequencies, or a series of position-velocity diagrams taken along different lines on the sky. These and several other very useful ways of displaying spectral line cubes are implemented in the `KARMA` package (Gooch 2000). It is important not to confuse the spectral line cube with an image of the line emission in three spatial dimensions, but often there is a velocity gradient along the line of sight due to the dynamics of the system which allows us to link some velocities with distances.

Another way to represent the data in the cube is by computing the velocity moments of the brightness. The nth moment map, $V^n(x, y)$ is defined by

$$V^n(x, y)\ \equiv\ \int_v T_B(x, y, v) \times (v - v_0)^n\ dv \tag{46}$$

where the cube is $T_B(x, y, v)$, v_0 is the systemic velocity or some appropriate zero point for the velocity scale, and the integral is taken as a sum over some

or all of the planes of the cube. The zero-th moment map is simply a map of the integral of the spectrum, as in equation 19 but taken for every spatial pixel. For the 21-cm line this gives column density (as long as the optical depth is not high). The first moment map shows the mean velocity (weighted by intensity) in each pixel. Often this gives a good image of the velocity field of the source. The second moment map generally shows the linewidth as a function of position. Examples of moment maps are shown on figure 6.

The first and higher order moment maps are very unstable to bias in the presence of noise. To be safe, the cube should be blanked to eliminate regions in both space and velocity which have no signal. This can be done by hand (the AIPS task BLANK is a good interactive tool for this), or automatically using a smoothed version of the cube as a template for determining where there is and is not signal. The AIPS task MOMNT is a good implementation of this strategy; it sets a threshold well outside the region with detected signal, so as to include the faint tails of strong lines, but it excludes spurious noise peaks in regions of the cube far from any emission.

The first moment map of a spectral line from the disk of a galaxy is generally used to fit the rotation velocity field. A good task for doing this is the GIPSY task ROCUR, which has been implemented on some AIPS systems. The objective is to determine several unknown parameters: the position of the center of the rotation pattern, the inclination (perhaps as a function of radius if the galaxy is warped) and the position angle of the major axis (i.e. the line of nodes, perhaps also as a function of radius), and the rotation curve, i.e. the circular velocity as a function of radius. The rotation curve is of critical importance for dynamical modelling since, with the assumption of circular rotation, it shows the distribution of gravitational force as a function of radius. Departures from circular rotation, e.g. in spiral arms, can often be analysed based on the first moment map as well.

Figure 6. [*See the jpeg file associated with this paper.*] Moment maps of M31 made from the WSRT synthesis data of Brinks and Shane (1984). The left figure is the zero moment, showing the HI column density, the center figure is the first moment, showing the radial velocity field, and the right figure is the second moment, showing the line width.

Fitting the parameters of the disk rotation gives a model velocity field which can be subtracted from the first moment map, leaving the velocity residual map. A good fit shows only noise in the residual map, but if the fit is not perfect, the residual map shows distinct patterns. Figure 7 shows some examples, taken from Warner, Wright, and Baldwin (1973).

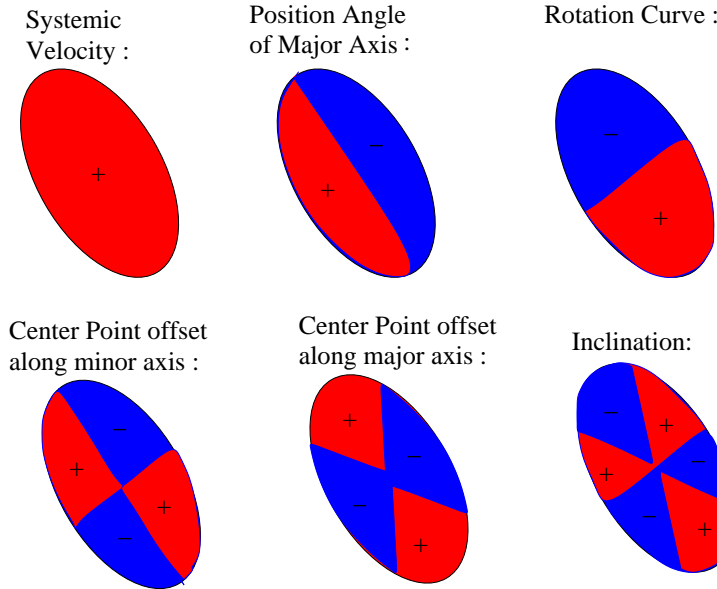## Residual Velocity Map – Signatures of Parameter Errors :

Figure 7. Errors in the fitted parameters give rise to patterns in the velocity residual map.

4.   Conclusions

Single dish telescopes are indispensible for observations of any spectral line source which is so extended that it cannot be imaged in a single interferometer field. The combination of single dish and aperture synthesis data is becoming the standard technique for mapping Galactic sources, especially for the ubiquitous HI line. Single dish telescopes like Arecibo and the GBT will be hugely valuable for this, particularly when equipped with multi-beam receivers to enhance their mapping speed. We may be on the threshold of a renaissance in single dish, Galactic, spectral line astronomy.

References

Bania, T.M., Balser, D.S., Rood, R.T., Wilson, T.L., and Wilson, T.J., 1997, Ap. J. Supp. 113, 353.

Brinks, E. and Shane, W.W., 1984, Astron. Astroph. Supp. 55, 179.

Caswell, J.L., 1997, MNRAS 289, 203.

Cornwell, T.J., 1988, A. & A. 202, 316.

Ekers, R.D. and Rots, A., 1979, in "Image Formation from Coherence Functions in Astronomy", ed. C. van Schooneveld, (Dordrecht : Reidel), p. 61.

English, J., Taylor, A.R., Irwin, J.A., Bougherty, S.M., Basu, S., et al. 1998, P.A.S.A. 15, 56.

Gibson, S.J., Taylor, A.R., Higgs, L.A., and Dedwney, P.E., 2000, Ap. J. 540, 851.

Lang, C.C., Goss, W.M., and Morris, M., 2001, Astron. J. 121, 2681.

Lewis, B.M., Oppenheimer, B.D., and Daubar, I.J., 2001, Ap. J. 548, L77.

Liszt, H. and Lucas, R., 1996, Astron. Astroph. 314, 917.

Magnani, L. and Onello, J.S. 1993, Ap. J. 408, 559.

McClure-Griffiths, N.M., Dickey, J.M., Gaensler, B.M., Green, A.J., Haynes, R.F., Wieringa, M.H., 2000, A.J. 119, 2828

McClure-Griffiths, N.M., Green, A.J., Dickey, J.M., Gaensler, B.M., Haynes, R.F., Wieringa, M.H., 2001, Ap.J. 551, 394.

Osterbrock, D.E., 1989, **Astrophysics of Gaseous Nebulae and Active Galactic Nuclei** (Sausalito : University Science Books).

Pauls, T., Johnston, K.J., and Wilson, T.L., 1996, Ap. J. 461, 223.

Peck, A.B., Goss, W.M., Dickel, H.R., Roelfsema, P.R., Kesteven, M., Dickel, J.R., Milne, D.K., and Points, S.D., 1997, Ap. J. 486, 329.

Phillips, C.J., Norris, R.P., Ellingsen, S.P., McColloch, P.M., 1998, MNRAS 300, 1131.

Rohlfs, and Wilson, T., 1996, **Tools of Radio Astronomy**, 2nd edition, (Berlin : Springer-Verlag).

Roshi, D.A., and Anantharamaiah, K.R., 1997, MNRAS 292, 63.

Sault, R.J., Staveley-Smith, L., and Brouw, W.N., 1996, A. & A. Supp., 120, 375.

Spitzer, L. 1977, **Physical Processes in the Interstellar Medium**, (New York : John Wiley).

Stanimirović, S. 1999, Ph.D. Thesis, University of Western Sydney Nepean, p. 157.

Szymczak, M., Kus, A.J., and Hrynek, G., 2000, MNRAS 312, 211.

Turner, B.E., 1998, Ap. J. 501, 731.

Warner, P.J., Wright, M.C.H., and Baldwin, J.E., 1973, MNRAS 163, 163.

Weaver, H. and Williams, D.R.W., 1973, Astron. Astrophys. Suppl., 8, 1.

This figure "Fig1.jpg" is available in "jpg" format from:

http://arXiv.org/ps/astro-ph/0107602v1

This figure "Fig2.jpg" is available in "jpg" format from:

http://arXiv.org/ps/astro-ph/0107602v1

This figure "Fig3.jpg" is available in "jpg" format from:

http://arXiv.org/ps/astro-ph/0107602v1

This figure "Fig4.jpg" is available in "jpg" format from:

http://arXiv.org/ps/astro-ph/0107602v1

This figure "Fig5a.jpg" is available in "jpg" format from:

http://arXiv.org/ps/astro-ph/0107602v1

This figure "Fig5b.jpg" is available in "jpg" format from:

http://arXiv.org/ps/astro-ph/0107602v1

This figure "Fig5c.jpg" is available in "jpg" format from:

http://arXiv.org/ps/astro-ph/0107602v1

This figure "Fig6.jpg" is available in "jpg" format from:

http://arXiv.org/ps/astro-ph/0107602v1

This figure "Fig7.jpg" is available in "jpg" format from:

http://arXiv.org/ps/astro-ph/0107602v1